CrossMark

ARTICLE

Chemical and boron isotopic composition of tourmaline from the Mariinsky emerald deposit, Central Urals, Russia

Ivan A. Baksheev[1] · Robert B. Trumbull[2] · Mikhail P. Popov[3,4] · Yuri V. Erokhin[3] · Olesya E. Kudryavtseva[5] · Vasily O. Yapaskurt[1] · Vera V. Khiller[3] · Galina M. Vovna[6] · Vladimir I. Kiselev[6]

Abstract Tourmaline is abundant at the Mariinsky schist-hosted emerald deposit in the Central Urals, Russia, both in emerald-bearing phlogopite veins (type 1) and later, emerald-free pockets, lenses, and veinlets cutting the phlogopite veins (type 2). The Ca content in tourmaline is influenced by the host rocks (ultramafic and mafic rocks), associated minerals, and minerals crystallized before tourmaline (amphibole, fluorite, margarite). The Na concentration in tourmaline depends on the presence or absence of paragonite, and the association with micas also strongly influences the contents of Li, Zn, Ni, and Co in tourmaline. Type 1 tourmalines associated with phlogopite are relatively depleted in these elements, whereas type 2 tourmalines associated with margarite or paragonite are enriched. Some differences in isomorphic substitutions along with the trace element composition (Zn, V, Sr, Co, REE) may have value in exploration of emerald-bearing and emerald-free veins in schist-hosted emerald deposits. The $\delta^{11}B$ values in tourmaline of all types fall in a narrow total range from -11.3 to $-8.4‰$. These values, combined with a mineralization temperature of 420–360 °C, yield an estimated $\delta^{11}B$ fluid composition of -7.4 to $-6.8‰$ suggesting a mixed source of boron, likely dominated from the granitic rocks surrounding the emerald belt. The narrow range of B-isotope compositions in tourmaline from throughout the Mariinsky deposit suggests a well-mixed hydrothermal system.

Editorial handling: B. Lehmann

✉ Ivan A. Baksheev
ivan.baksheev@gmail.com

1   Geology Department, Moscow State University, Leninskie Gory, Moscow 119991, Russia

2   GFZ German Research Centre for Geosciences, Telegrafenberg, 14473 Potsdam, Germany

3   Institute of Geology and Geochemistry, Urals Branch, Russian Academy of Sciences, ul. AkademikaVonsovskogo15, Yekaterinburg 620016, Russia

4   Urals State Mining University, ul. Kuibysheva 30, Yekaterinburg 620144, Russia

5   GemsMuseum, ul. Narodnogo Opolcheniya 29/1, Moscow 123154, Russia

6   Far East Geological Institute, Far East Branch, Russian Academy of Sciences, pr. 100-letiya Vladivostoka 159, Vladivostok 690022, Russia

Introduction

At present, two major types of economic emerald deposits are known: "Colombian" and "schist-hosted." The Colombian-type deposits provide about 60% of the world emerald production (Groat et al. 2008). They are hosted in weakly metamorphosed, pyrite-bearing carbonaceous limestone sequences and are located predominantly in Colombia. The schist-hosted emerald deposits are much more widespread and geologically diverse. They are hosted in medium to high-grade schists derived from, or spatially related to, ultramafic rocks and are in most cases also associated with granitic intrusions. The subject of this paper is the "type example" of schist-hosted deposits, in the Urals Mountains of Russia, first described by Fersman (1925). Other examples in the literature include Habachtal, Austria (Grundmann and Morteani 1989); Swat

Valley, Pakistan (Arif et al. 1996); Tsa da Glisza, Yukon Canada (Groat et al. 2002); Kafubu, Zambia (Seifert et al. 2004); Carnaiba, Brazil (Giuliani et al. 1990); and Leydsdorp, South Africa (Grundmann and Morteani 1989). The origin of the schist-type emerald deposits has been debated since their first description, with the essential disagreement being the relative importance of magmatic versus metamorphic processes, and specifically the role of granitic fluids. It is now generally accepted that the deposits are essentially metamorphic/metasomatic in origin and that granitic or pegmatitic rocks play an important role as the source of beryllium, although this model does not require that granitic magmas are directly involved (Grundmann and Morteani 1989; Arif et al. 1996; Trumbull et al. 2009; Kupriyanova and Sokolov 1984; Spiridonov 1998; Seifert et al. 2004; Zachariáš et al. 2005; Groat et al. 2008; Schmid 2001; Fersman 1925; Vlasov and Kutukova 1960; Kupriyanova 2002).

The classic Emerald Mines locality in the Central Urals, 80 km north of Yekaterinburg (Fig. 1), has attracted many geological and mineralogical studies (Ginzburg 1959; Beus 1966; Vlasov and Kutukova 1960; Sherstyuk and Kozlov 1976; Zolotukhin 1999; Gavrilenko 2003; Zhernakov 2009). Most of the mineralogical studies were purely descriptive or concerned mainly with the genesis of beryl itself. Details and reliable data about the chemical composition of other minerals associated with emeralds in the Urals deposits are rare in the literature, but from other studies, it is known that the accompanying minerals can be of value for clarifying the genesis of the deposit and/or for use as proximity indicators of emerald mineralization. One of the most abundant and potentially most useful of these is tourmaline because of its wide chemical variability, stability, and ability to constrain fluid provenance (Trumbull et al. 2009; Galbraith et al. 2009). A few previous studies of tourmaline from the Urals Emerald Mines district have reported major-element compositions, but these data are published in local Russian literature (Baksheev et al. 2002, 2003; Kudryavtseva et al. 2004) or academic theses (Gavrilenko 2003) and are not accessible internationally. This paper presents a detailed geochemical study of tourmaline from the famous Mariinsky deposit (also known as Mariinskoe, Mariinsk, Malyshevo, Malyshev, Malyshevsk, Malyshevskoe), which is the largest and still-active deposit in the Emerald Mines district. We also analyzed one sample from the inactive Krasnoarmeisky deposit in the southern part of the district. The data set presented here combines major-element data from previous work with new electron microprobe analyses from this study. In addition, we report for the first time trace-element compositions determined by laser ablation-inductively coupled mass spectrometry (LA-ICP-MS) and boron-isotope compositions determined by secondary ion mass spectrometry (SIMS).

Regional and deposit geology

The Ural emerald mining district (Ural emerald belt) is located between the Eastern Urals upland and the Eastern Urals depression. The emerald belt is bordered to the west by the Precambrian sialic block and metamorphic rocks of the Murzinka–Adui microcontinent. To the east is the Early Silurian Rezh (Tolmachevo–Asbest) volcanic zone, which comprises island arc and oceanic complexes. Several granitic intrusions occur in and around the Ural emerald belt. On the west is the Adui granite pluton (250–290 Ma according to Fershtater et al. 2007), which extends for 39 km north–south (Fig. 1). The Adui pluton shows irregular internal zoning, with the first-phase granites at the pluton margin on its western flank, second-phase granites in the central part, and an eastern part of the pluton dominated by leucocratic granite. The southern border of the Ural emerald belt contacts the Kamenka granite pluton (Fig. 1) whose age is 297 ± 2.2 Ma (Fershtater et al. 2007). Both the Kamenka and Adui granites are cut by veins and dykes of leucocratic granite, pegmatite, and aplite. An older, more mafic intrusion, the Middle Devonian Lesozavodsk diorite (Popov 2014), bounds the Ural emerald belt in the east (Fig. 1). Finally, on the northeast, the emerald belt is in contact with the Malyshevo granite pluton (Fig. 1), aged 260 Ma (Popov et al. 2003). According to Popov et al. (2003), the youngest intrusions within the emerald belt are the NYF (niobium-yttrium-fluorine)-type microcline–albite pegmatites of the Kvartalnoe deposit containing columbite, tantalite, euxenite, xenotime, synchysite, beryl, monazite, and uraninite (Khiller et al. 2015) and located 15 km south of the Mariinsky deposit in the southern Emerald belt (Fig. 1). Popov et al. (2003) dated the pegmatites by the Rb/Sr method at 196.5 ± 1.9 Ma. However, Khiller et al. (2015) determined an older age of these pegmatites by Th–U–Pb chemical dating of monazite and uraninite at 267.9 ± 2.1 Ma. This discrepancy in ages is not yet resolved, but we note that the older date of Khiller et al. (2015) agrees with published ages of the Adui granite, whereas the Jurassic Rb–Sr age of Popov et al. (2003) is not supported by other known manifestations of Jurassic magmatism in the Emerald Mine district and in the central Urals.

The rocks within the Ural emerald belt are part of a N–S to NW–SE striking amphibolite facies volcano-sedimentary sequence of Neoproterozoic to Middle Cambrian age (Zhernakov 2009), which is intruded by ultramafic bodies related to the Late Silurian to Devonian Bazhenovsky dunite–harzburgite massif. The ultramafic bodies have in most cases been transformed to serpentinites with chrysotile, lizardite, and antigorite varieties. The serpentinites in turn are transformed into talc, talc-tremolite, and talc-actinolite schists along faults. Finally, in addition to the ultramafic bodies, the volcano-sedimentary sequence has been intruded by diorite dykes related to the Middle Devonian Lesozavodsk Pluton.
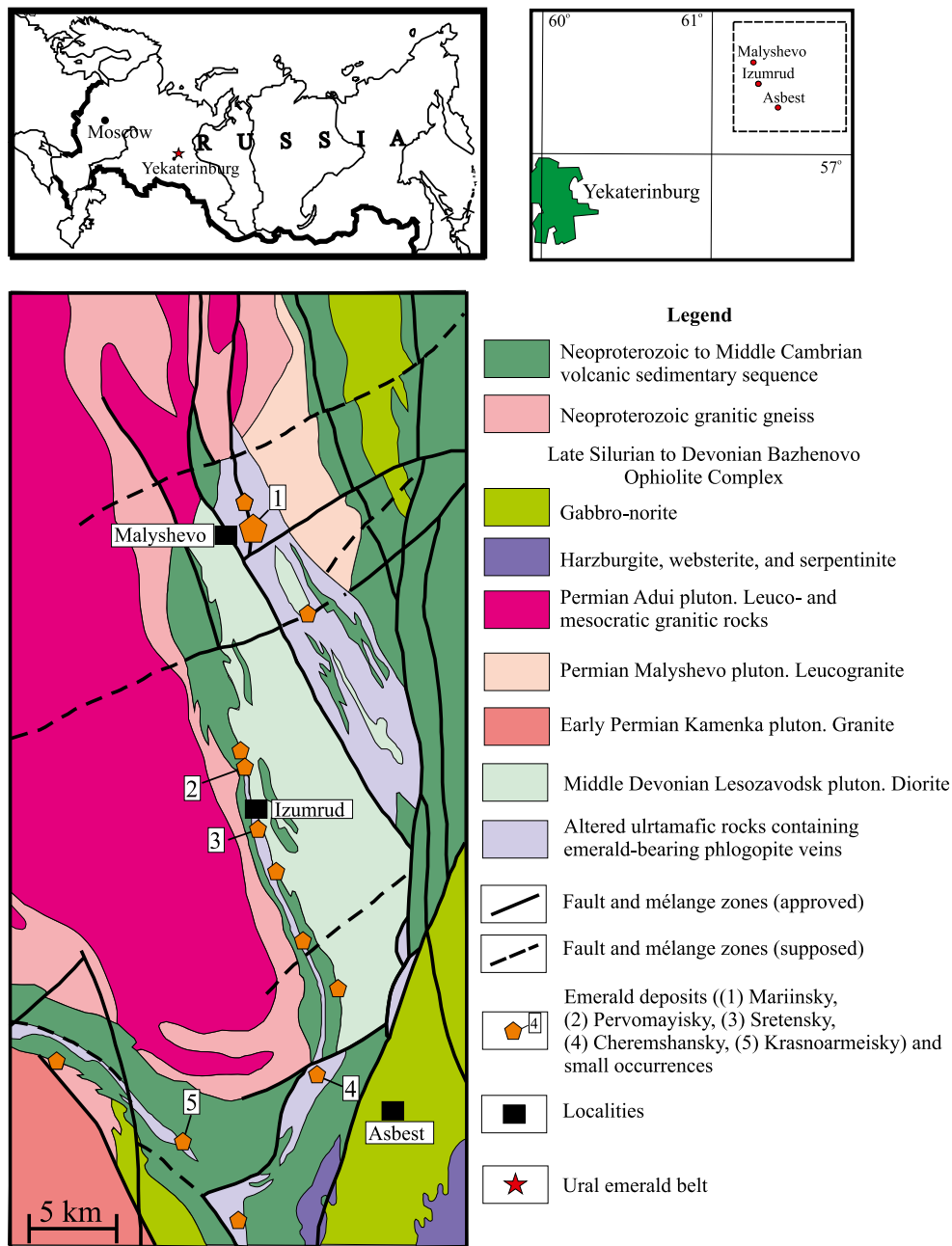
Fig. 1 Geographical location and simplified geological map of the Ural emerald belt, modified after Popov et al. (2008)

Mariinsky is the largest deposit of emerald, alexandrite, and phenakite in the Ural emerald belt (Zhernakov 2009). The deposit is located in a zone of serpentinite mélange between the Adui and Malyshevo plutons (Fig. 1). The major ore-controlling and ore-hosting structures are three faults and spatially related diorite dikes (Fig. 1). The Mariinsky ore zone dips to the south at 50°. It has been traced along strike for 1.1 km (at 120 m below surface) (Fig. 2) and extends at depth to 360–500 min underground workings. The orebodies consist of emerald-bearing phlogopite schist and of late emerald-free but Cr-free beryl-bearing quartz–plagioclase veins. The phlogopite bodies are lens-shaped, typically with less than

50 m extent along strike (occasionally 100 m) and down dip, and with a thickness range from 0.2 to 8.5 m. The major minerals in the phlogopite bodies are phlogopite, chlorite, actinolite, plagioclase, beryl (including emerald), and tourmaline.

Concerning the age of emerald-bearing schist, there are two conflicting results. According to Bidny et al. (2011) and Popov et al. (2003), the Rb/Sr age of the schist is 206.6 ± 1.4 and 207 ± 5.2 Ma, respectively, which is close to the Rb/Sr age of 196.5 ± 1.9 Ma for the Kvartalnoe pegmatites by Popov et al. (2003). In contrast, Kupriyanova (2002) reported a K/Ar age of phlogopite from phlogopite schist of
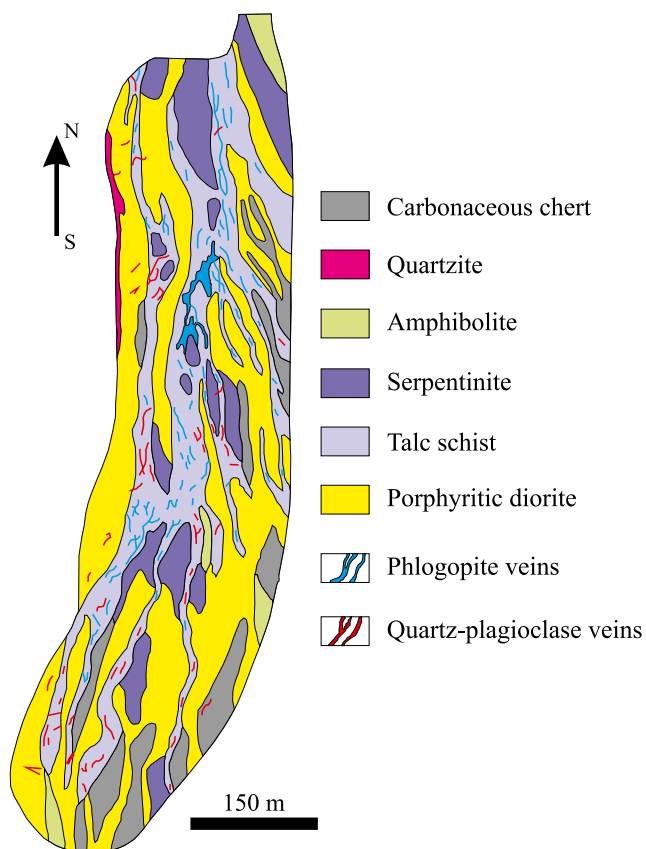
Fig. 2 Geological sketch map of the Mariinsky deposit at a depth of −220 m, modified after Zolotukhin ([1996])

269 ± 6 Ma, which is close to the U–Pb age of 267.9 ± 2.1 of the Kvartalnoe pegmatites determined by Khiller et al. ([2015]). There is currently no solution to this age discrepancy, but both sets of data suggest a close temporal relationship between NYF pegmatites and formation of the ultramafic schist.

The quartz–muscovite–plagioclase veins in the Mariinsky deposit occur along NE-trending faults and dip to the south or north at low angles. They reach 50 m in length and have thicknesses from 0.5 to 5 m. The veins are composed mainly of quartz and plagioclase, with minor muscovite, margarite, fluorite, tourmaline, apatite, beryl, and molybdenite. Where the veins intersect phlogopite bodies in fault zones, they display contact metasomatic zones toward vein consisting of margarite, muscovite, fine-grained oligoclase, and coarse-flake muscovite.

The inactive Krasnoarmeisky (also known as Krasnoarmeiskoe, Krasnoarmeisk, Khitny) deposit is situated in the southern Ural emerald belt (Fig. [1]) in a zone of serpentinite melange hosted in intercalated pyroxene amphibolite, carbonaceous shales, and actinolite and chlorite schists at the distance 1.8 km of the contact with the Adui Pluton. Ultramafic rock is talc schist with lenses of serpentinite. In addition to the ultramafic bodies, this sequence contains concordant diorite bodies.

The orebodies consist of emerald-bearing phlogopite schist and pegmatites. Phlogopite bodies are the most abundant in the central part of the deposit. They are spatially separated, 0.25–3 m thick, irregular in strike, and complexly branched. In the central and eastern parts, these bodies are traced to the 180 m depth below surface. The mineral assemblage in the phlogopite bodies is similar to that of the Mariinsky deposit. Pegmatites are abundant in the eastern part of the deposit, where they form thick fractionated dikes (up to 100 m along striking and up to 20 m in thickness) enriched in beryl, molybdenite, and columbite-tantalite. These dikes can be both concordant and discordant with regard to the host sequence. No spatial relations were found between pegmatites and emerald-bearing bodies.

Sampling and petrographic descriptions

The tourmaline samples collected for this study represent the two main types of tourmaline-bearing rocks at the Mariinsky and Krasnoarmeisky deposit. Type 1 hosts collected from both Mariinsky and Krasnoarmeisky are early-formed emerald- and beryl-bearing phlogopite schist (glimmerite) bodies, whereas type 2 hosts collected only from Mariinsky are later quartz–plagioclase pockets, lenses, and veinlets hosted in or cross-cutting glimmerite, which are emerald- and beryl-free. These two rock types are further subdivided according their main mineral assemblage, with the nature of tourmaline within them and the sample numbers in this study explained below. The distribution of samples selected is shown on an idealized sketch in Fig. [3].

Type 1a: phlogopite–tourmaline veins (M-8, M-102)

These brownish emerald-bearing schistose veins are the most abundant emerald hosts at the Mariinsky deposit. They are 0.2–0.7 m thick and 40–100 m long, cutting serpentinized ultramafic bodies. The veins are composed almost entirely of phlogopite (60%) and tourmaline (40%), with minor plagioclase, serpentine, talc, emerald, green and pale green beryl, and relict chrome spinels. Tourmaline occurs typically as individual brown crystals ranging in size from a few millimeters to 3 cm in length and up to 1 cm in width, and as intergrowths of three to six crystals (Fig. [4]a). Tourmaline grains are oriented along the schistosity and commonly show transverse fractures cemented by phlogopite and a fine-grained aggregate of quartz, plagioclase, rutile, and sulfides (Fig. [4]a). Locally, tourmaline forms sheaf-like or radial aggregates up to 2.5 cm in diameter. Tourmaline crystals are closely intergrown with phlogopite.
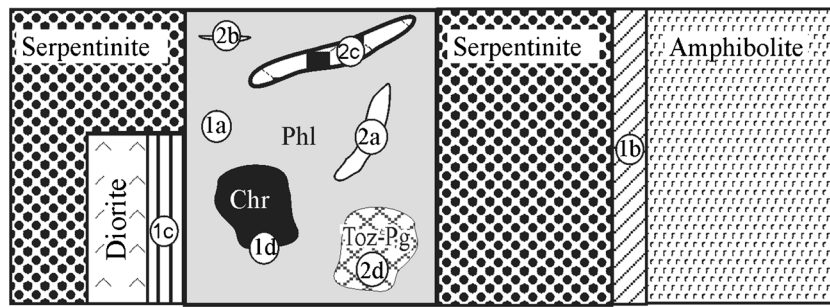
Fig. 3 Schematic sketch of zones between serpentinite and amphibolite showing the types of tourmaline-bearing samples discussed in this study (*circled symbols*—see text for explanation). *Phl* phlogopite–tourmaline vein, *Chr* chromitite pocket, *Toz-Pg* topaz–paragonite pocket

Type 1b: phlogopite–tourmaline–tremolite veins (M-104)

These greenish brown, schistose emerald-bearing veins occur at the contact between serpentinized ultramafic bodies and amphibolites. They are about 0.1–1.5 m thick and 8–14 m long and consist of phlogopite (45%), tourmaline (30%), and tremolite (25%), with minor chlorite, quartz, plagioclase, emerald, and green and pale green beryl. Tourmaline in these rocks occurs as black crystals up to 1 cm long oriented along the schistosity of the rock and closely intergrown with phlogopite. Small inclusions of phlogopite and plagioclase occur in the tourmaline cores and, less commonly, in the rims.

Type 1c: plagioclase–phlogopite–tourmaline veins (KA-5)

These veins occur at the Krasnoarmeisky deposit at the contact between emerald-bearing phlogopite veins and diorite bodies. The veins are 0.2 to 6 m long and 20 to 30 cm thick, and they comprise cream-white plagioclase (70%), gray (15%), and black tourmaline (15%); minor constituents are chlorite, quartz, and magnetite. The tourmaline crystals are 2 to 4 cm in length and 2 to 4 mm across, occasionally forming radial aggregates. Tourmaline is predominantly localized at the contact between plagioclase and phlogopite.

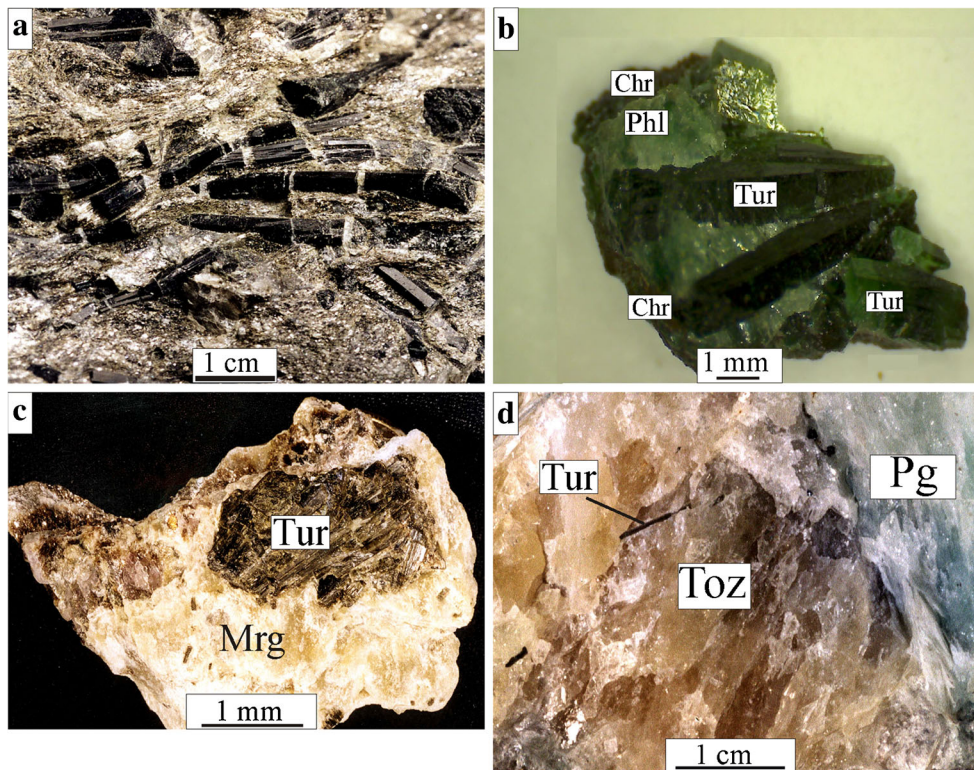**Fig. 4** Photographs illustrating various types of tourmaline from Mariinsky. **a** Brecciated crystals of type 1a tourmaline cemented by brown fluor-phlogopite. **b** Three-grain cluster of green tourmaline crystals with interstices filled by green fluor-phlogopite. **c** Type 2c tourmaline with margarite. **d** Type 2d tourmaline with topaz. *Chr* chromite, *Mrg* margarite, *Pg* paragonite, *Toz* topaz, *Tur* tourmaline

Type 1d: chromite–phlogopite–paragonite–tourmaline alteration zone (BAK-1)

This green, fine- to medium-grained rock occurs at the contact between chromitite and tourmaline–phlogopite veins. It is composed of chromite (80%), fluor-phlogopite and paragonite (19%), tourmaline (1%), and minor mariinskite (Cr analog of chrysoberyl). Eskolaite (Cr_2O_3), fluorapatite, and zircon are accessories. Tourmaline cuts paragonite and forms fractured crystals and sheaf-like clusters cemented by later fluor-phlogopite and locally replacing chrome spinel (Fig. 4b). The tourmaline crystals are up to 8 mm in length and optically zoned, with a green core and light brown rim.

Type 2a: tourmaline–phlogopite–plagioclase–quartz pockets (Chb, M-127)

These emerald-free segregations of black tourmaline (30–50%), gray phlogopite (20–30%), light gray to yellow plagioclase (15–20%), and quartz (5%) are 3–8 cm in diameter and located in the central and marginal parts of type 1 phlogopite–tourmaline veins. Dark brown prismatic tourmaline crystals a few millimeters to a few centimeters long are randomly oriented in a quartz–phlogopite–plagioclase matrix.

Type 2b: tourmaline–fluorite veinlets (M-112)

These emerald-free veinlets cross-cut type 1 phlogopite–tourmaline veins. They are 3–12 cm long and 1–5 cm thick. Tourmaline occurs as greenish brown, isolated crystals up to 2.5 cm in length and as sheaf-like aggregates. The crystals are typically fractured and cemented by violet fluorite and phlogopite.

Type 2c: margarite–tourmaline veinlets (M-115, M-131, M-134)

Margarite (50–80%) and tourmaline (20–50%) are the major constituents of veins and veinlets a few centimeters to 3 m long and up to 50 cm thick, which cross-cut type 1 phlogopite–tourmaline veins (Fig. 4c). Albite, phlogopite, chlorite, and bluish corundum are minor constituents in these emerald-free veins. Tourmaline forms light brown elongated crystals up to 0.5 cm long and rounded clusters up to 5 cm in diameter. The boundaries between tourmaline and margarite grains are smooth with no indication of a reaction relation.

Type 2d: tourmaline–topaz–paragonite lenses (M-119)

These emerald-free tourmaline–topaz–paragonite lenses occur in phlogopite–tourmaline veins of type 1. They reach 70 cm in thickness and 80–120 cm in length and are zoned, with yellowish topaz-rich cores and rims of fine-grained paragonite (Zhernakov 1998). Locally, topaz has been completely replaced by paragonite. Tourmaline in this setting occurs as dark green or brown crystals from 2 to 7 mm in length included in topaz (Fig. 4d).

Analytical techniques

Electron microprobe analyses

The chemical composition of tourmaline was determined on polished epoxy grain mounts of tourmaline separates with a JEOL JSM-6480LV electron microscope equipped with an Inca Energy-350 energy dispersion system (EDS) and Inca Wave-500 wavelength dispersion system (WDS) at the Laboratory of Analytical Techniques of High Spatial Resolution, Department of Petrology, Moscow State University, and with a Cameca SX-100 electron microprobe using WDS at the Institute of Geology and Geochemistry Urals Branch, Russian Academy of Sciences in Yekaterinburg. The JEOL electron microscope was operated at an accelerating voltage of 15 kV and a beam current of 20 nA. The EDS detector was used for all elements except F, employing natural silicate reference minerals (Jarosewich 2002) for calibration. Uncertainty of single measurements of oxides does not exceed 1.5% relative. Fluorine concentrations were measured with WDS (TAP crystal), using MgF_2 as a reference standard. The XPP (eXtended Pouchou&Pichoir) corrections were used for correction (program "INCA" version 17a). The Cameca electron microprobe was operated at an accelerating voltage of 15 kV and a beam current of 50 nA. The following mineral standards were used: diopside (Si, Ca, Mg), orthoclase (Al, K), jadeite (Na), Fe_2O_3 (Fe), TiO_2 (Ti), Cr_2O_3 (Cr), rhodonite (Mn), and fluor-phlogopite (F). Uncertainty of single measurements of oxides does not exceed 1% relative. The PAP (Pouchou&Pichoir) corrections were used for correction procedures.

Tourmaline formulae were calculated on the basis of 15 cations at the tetrahedral and octahedral sites (T, Z, and Y) exclusive of Na, Ca, and K, which is appropriate for low-Li tourmaline as expected in rocks of the type studied here (Henry et al. 2011). All iron was assumed to be Fe^{2+}. Charge-balance constraints were used to estimate the amounts of OH^- and O^{2-} in the V and W anion sites. We recognize that there are significant uncertainties with these estimates (Dutrow and Henry 2000). The calculated O^{2-} is preferentially assigned to the W site together with F (Henry et al. 2011). The proportion of X site vacancies (□) was calculated as [1 − (Na + Ca + K)]. The concentration of B_2O_3 was calculated from stoichiometric constraints assuming 3 B apfu. Selected analyses are given in Table 1.

Table 1 Representative electron microprobe data for Mariinsky tourmaline

Component	M-8	M-104	KA-5	BAK-1	BAK-1	M-127	M-112	M-115	M-119
	1a	1b	1c	1d (1)	1d (2)	2a	2b	2c	2d
B_2O_3[a] wt.%	10.48	10.49	10.69	10.79	10.50	10.72	10.62	10.65	10.72
SiO_2	35.67	36.20	36.51	36.31	34.41	36.56	36.18	36.34	36.74
TiO_2	0.44	0.60	0.40	bdl	0.01	0.23	0.25	0.06	0.14
Cr_2O_3	bdl	0.05	0.24	0.82	19.56	bdl	bdl	bdl	0.17
V_2O_3	0.05	0.09	0.09	bdl	bdl	0.05	0.06	bdl	0.06
Al_2O_3	31.33	31.16	30.52	33.37	21.28	32.67	32.34	34.05	34.48
NiO	bdl	bdl	bdl	0.30	na	bdl	bdl	bdl	bdl
FeO	5.81	3.31	4.51	0.16	0.17	4.64	7.18	5.73	5.39
MnO	0.05	bdl	bdl	bdl	bdl	0.10	0.07	0.10	0.07
MgO	8.44	9.58	10.31	11.06	7.66	8.91	7.43	7.03	6.87
CaO	1.11	1.18	2.20	0.94	0.40	0.66	0.36	0.25	0.32
Na_2O	2.33	2.24	1.75	2.29	2.49	2.63	2.68	2.39	2.07
F	1.28	0.05	1.07	1.43	0.18	1.20	1.25	0.95	0.54
H_2O[a]	2.76	2.71	2.76	2.80	2.88	2.77	2.75	2.75	2.77
2F = O	−0.54	−0.02	−0.45	−0.31	−0.08	−0.50	−0.53	−0.40	−0.23
Total	99.21	97.64	100.60	99.94	99.46	100.64	100.64	99.90	100.11
Formulae calculated on basis of 15 cations									
Si	5.916	5.996	5.936	5.846	5.964	5.927	5.920	5.932	5.956
^{T}Al	0.084	0.004	0.064	0.154	0.306	0.073	0.080	0.068	0.044
Total T	6.000	6.000	6.000	6.000	6.000	6.000	6.000	6.000	6.000
^{Z}Al	6.000	6.000	5.786	6.000	3.844	6.000	6.000	6.000	6.000
^{Z}Cr					1.574				
^{Z}Mg			0.214		0.582				
Total Z	6.000	6.000	6.000	6.000	6.000	6.000	6.000	6.000	6.000
^{Y}Al	0.040	0.080		0.179		0.169	0.157	0.484	0.546
^{Y}Mg	2.087	2.366	2.286	2.655	1.308	2.154	1.812	1.712	1.660
Fe^{2+}	0.806	0.458	0.613	0.022	0.024	0.630	0.983	0.783	0.732
Ti	0.054	0.075	0.049		0.001	0.028	0.030	0.008	0.017
^{Y}V	0.006	0.012	0.012			0.006			0.007
^{Y}Cr		0.008	0.040	0.104	1.667				0.028
Mn	0.007						0.013	0.010	0.014	0.009
Ni				0.039					
Total Y	3.000	2.999	3.000	2.999	3.000	3.000	3.000	3.001	2.999
Na	0.751	0.718	0.551	0.715	0.799	0.826	0.851	0.757	0.651
Ca	0.198	0.209	0.384	0.162	0.071	0.115	0.063	0.044	0.055
X-vac	0.051	0.073	0.065	0.123	0.130	0.059	0.086	0.199	0.294
Total X	1.000	1.000	1.000	1.000	1.000	1.000	1.000	1.000	1.000
F	0.672	0.026	0.550	0.728	0.094	0.615	0.647	0.489	0.277
^{W}OH	0.110	0.591	0.260	0.101	0.184	0.170	0.231	0.234	0.389
^{W}O	0.278	0.383	0.190	0.171	0.722	0.215	0.122	0.277	0.334
Total W	1.000	1.000	1.000	1.000	1.000	1.000	1.000	1.000	1.000
Al_{tot}	6.124	6.084	5.850	6.333	4.150	6.242	6.237	6.552	6.590
Fe/(Fe + Mg)	0.28	0.16	0.20	0.01	0.01	0.23	0.35	0.31	0.31
Ca/(Ca + Na)	0.21	0.23	0.41	0.18	0.08	0.12	0.07	0.05	0.08

bdl denotes the element content is below detection limit by electron microprobe. *na* denotes the element was not analysed. *(1)* and *(2)* denote first and second groups of subtype 1d tourmaline, respectively

[a] B_2O_3 and H_2O contents calculated by stoichiometry

Trace element analyses

In situ analyses of trace elements in tourmaline were performed by laser ablation ICP-MS at CODES, University of Tasmania, and at the Far Eastern Geological Institute, Russian Academy of Sciences, in Vladivostok. Selected analyses are given in Table 2.

The instrumentation at CODES includes a RESOlution S-155193 nm excimer laser probe, coupled to an Agilent 7700s quadrupole mass spectrometer. Samples were ablated in an atmosphere of pure He, then the He carrier gas (0.35 l/min) was mixed with Ar (1.05 l/min) immediately after the ablation cell. Analyses were conducted using the spot mode, whereby the sample remains stationary under the laser beam. Each analysis lasted 90 s, including 30 s of background acquisition (laser off) followed by 60 s of ablation. A 32-μm-diameter beam was used (3.5 J.cm^2; 20 nm pulse width) with laser frequency of 10 Hz. The mass spectrometer was tuned to

increase sensitivity on medium to high masses. Dwell time for each mass was 20 ms, resulting in the total sweep time of 0.9 s, and 65 sweeps were recorded during each ablation. Primary and secondary standards analyzed prior to and after the tourmaline samples were used to correct for instrument drift and matrix effects. Data reduction was performed based on an ideal 97 wt.% analytical sum (water-free) as the internal standard value (Longerich et al. 1996).

The instrumentation at Far Eastern Geological Institute includes an Agilent 7500a inductively coupled plasma mass spectrometer joined with the laser ablation system of the NWR-213 type. The N.I.S.T. SRM610 standard was analyzed prior to and after the tourmaline samples, and used to correct for instrument drift and matrix effects. Samples were ablated in an atmosphere of pure He, then the He carrier gas (0.85 l/min) was mixed with Ar (0.9 l/min) immediately after the ablation cell. Analyses were conducted using spot mode, each analyses lasting 80 s,

Table 2   Selected trace element composition of tourmaline from Mariinsky

Component	M-102	M-104	KA-5	BAK-1	M-127	M-112	M-131	M-119
	1a	1b	1c	1d	2a	2b	2c	2d
Li, ppm	6.87	59	216	156	257	382	232	112
Be	0.77	0.85	11	3.77	7.66	45	12	12
Sc	36	6.39	22	n.a.	8.06	13	12	7.95
V	320	382	349	294	111	131	253	183
Co	18	19	32	bdl	42	43	60	90
Ni	97	206	600	1457	501	217	327	1751
Cu	bdl	0.43	bdl	0.47	0.79	0.52	0.57	bdl
Zn	35	29	160	3.74	473	693	448	267
Ga	26	30	86	3.48	54	55	54	43
Ge	0.90	0.60	2.21	2.64	2.74	3.40	4.58	3.76
Sr	1724	1084	1764	489	286	378	368	39
Y	0.03	0.26	0.05	0.09	bdl	bdl	0.03	bdl
Zr	0.07	44[a]	bdl	bdl	bdl	bdl	bdl	bdl
Nb	bdl	bdl	0.21	0.12	0.06	0.25	bdl	bdl
Sn	3.05	1.99	4.30	3.00	1.31	1.55	2.45	2.01
Cs	bdl	bdl	bdl	bdl	bdl	bdl	bdl	0.42
Ba	bdl	0.47	0.43	bdl	bdl	bdl	bdl	bdl
La	1.46	1.46	0.20	0.46	2.54	7.95	4.51	0.43
Ce	2.31	2.23	0.29	0.69	4.37	14	7.81	0.77
Pr	0.18	0.13	0.03	0.05	0.37	1.34	0.74	0.07
Nd	0.75	0.32	0.10	0.10	1.00	4.24	2.40	0.21
Sm	0.10	bdl	bdl	0.09	0.11	0.31	0.17	bdl
Eu	0.56	0.49	0.41	0.08	0.32	0.40	0.63	0.05
Gd	0.10	bdl	bdl	0.06	bdl	0.11	0.07	bdl
Tb	bdl	bdl	bdl	bdl	bdl	0.01	bdl	bdl

Single-spot analyses are given. Sample BAK-1 was analyzed at the Far Eastern Geological Institute, Russian Academy of Sciences, in Vladivostok. All other samples were measured at CODES, University of Tasmania

[a] Many zircon inclusions

including 20 s of background acquisition (laser off) followed by 60 s of ablation. A 40-μm-diameter beam was used (5.5 J cm^2) with laser frequency of 10 Hz. The mass spectrometer was tuned to increase sensitivity on medium to high masses. Dwell time for each mass was 10 ms, resulting in the total sweep time of 0.89 s, and 67 sweeps were recorded during each ablation. The measured values were treated using Glitter v. 4.4.2 software (Access Macquarie Ltd).

Boron isotope analyses

B-isotope analyses were performed with the Cameca 1280-HR SIMS instrument at the German Research Centre for Geosciences (GFZ) in Potsdam on the same mounts previously analyzed by microprobe and LA-ICP-MS. Prior to SIMS analyses, the samples were cleaned with ethanol in an ultrasonic bath, then sputter coated with 35 nm of high-purity gold. The SIMS analyses employed a 5.5-nA, $^{16}O^-$ primary ion beam with an energy of 13 keV, with a beam diameter of 5 μm. Positive secondary ions were extracted using a +10 kV potential, with no offset voltage. Each analysis was preceded by a 90-s pre-sputtering to remove the gold coat and establish stable sputter conditions. The analyses were done in multicollection mode with faraday cups, and consisted of 20 cycles with 4 s integration time per cycle. The mass resolution of the instrument was $M/\Delta M \approx 2000$, which is more than adequate to separate the $^{11}B^+$ and $^{10}B^1H^+$ mass stations. The typical count rate for $^{11}B^+$ under these conditions was about 2×10^7 ions per second. Correction for instrumental

mass fractionation (IMF) and monitoring uncertainty was done with multiple analyses of tourmaline reference materials (RMs) Harvard 112566 schorl and Harvard 108796 dravite (Dyar et al. 2001). The results from single analyses yielded within-run uncertainties of 0.1 to 0.2‰ (1 SD). Analytical repeatability on individual RMs was <0.5‰ (1 SD). The variability of IMF values for all analyses from both RMs was <0.7‰ (1 SD), which is our estimate for the overall reliability of the data. After correction for the mean value of IMF for all RMs, the measured $^{11}B/^{10}B$ ratios were converted to $\delta^{11}B$ values and are calculated relative to the NBS SRM-951 value of 4.04362 (Catanzaro et al. 1970).

Analyses were made on polished grain mounts, with two to three points in each tourmaline grain with the exception of sample BAK-1 ($n = 11$). The range of boron isotopic composition for each sample is given in Table 3.

Results

Major element variations and substitution vectors

The chemical compositions of the tourmaline analyzed in this study are combined with earlier data on the major-element plots. Figure 5 compares tourmaline of type 1 (left panels) and type 2 (right) in terms of the ternary classification diagrams from Henry et al. (2011). On the ternary plot of X-site occupancy (Fig. 5a, b), both type 1 and type 2 tourmaline plot in the alkali field, but they differ in that type 1 tends toward higher concentrations of Ca and less site vacancies than type

Table 3 Summary of boron isotope composition of tourmaline from the Mariinsky deposit

Sample	Host rock type and assemblage	$\delta^{11}B$ (‰)	Number of analyses
Type 1			
M-8	1a: Phl–Tur vein	−10.4/−10.4	2
M-102	1a: Phl–Tur–Tlc vein	−9.6/−9.3	2
M-104	1b: Phl–Tur–Tr vein	−10.6/−10.5	2
KA-5	1c: Pl–Phl–Tur vein	−10.8/−10.8/−10.9	3
BAK-1	1d: Chr–Phl–Pg–Tur alteration	−10.1 ± 0.8	11
Type 2			
Chb	2a: Tur–Phl–Pl–Qz pocket	−10.0/−10.0	2
M-127	2a: Tur–Phl–Pl–Qz pocket	−11.0/−10.5	2
M-112	2b: Tur–Fl veinlet	−10.8/−10.5	2
M-115	2c: Mrg–Tur veinlet	−11.1/−10.8	2
M-131	2c: Mrg–Tur veinlet	−9.8/−9.7	2
M-134	2c: Mrg–Tur veinlet	−9.1/−8.9	2
M-119	2d: Tur–Toz–Pg lens	−8.9/−8.9	2

B-isotope analyses by SIMS, uncertainty 0.7‰ (1 SD)

Mineral abbreviations: *Chr* chromite, *Fl* fluorite, *Mrg* margarite, *Pg* paragonite, *Phl* phlogopite, *Pl* plagioclase, *Tlc* talc, *Toz* topaz, *Tr* tremolite, *Tur* tourmaline, *Qz* quartz
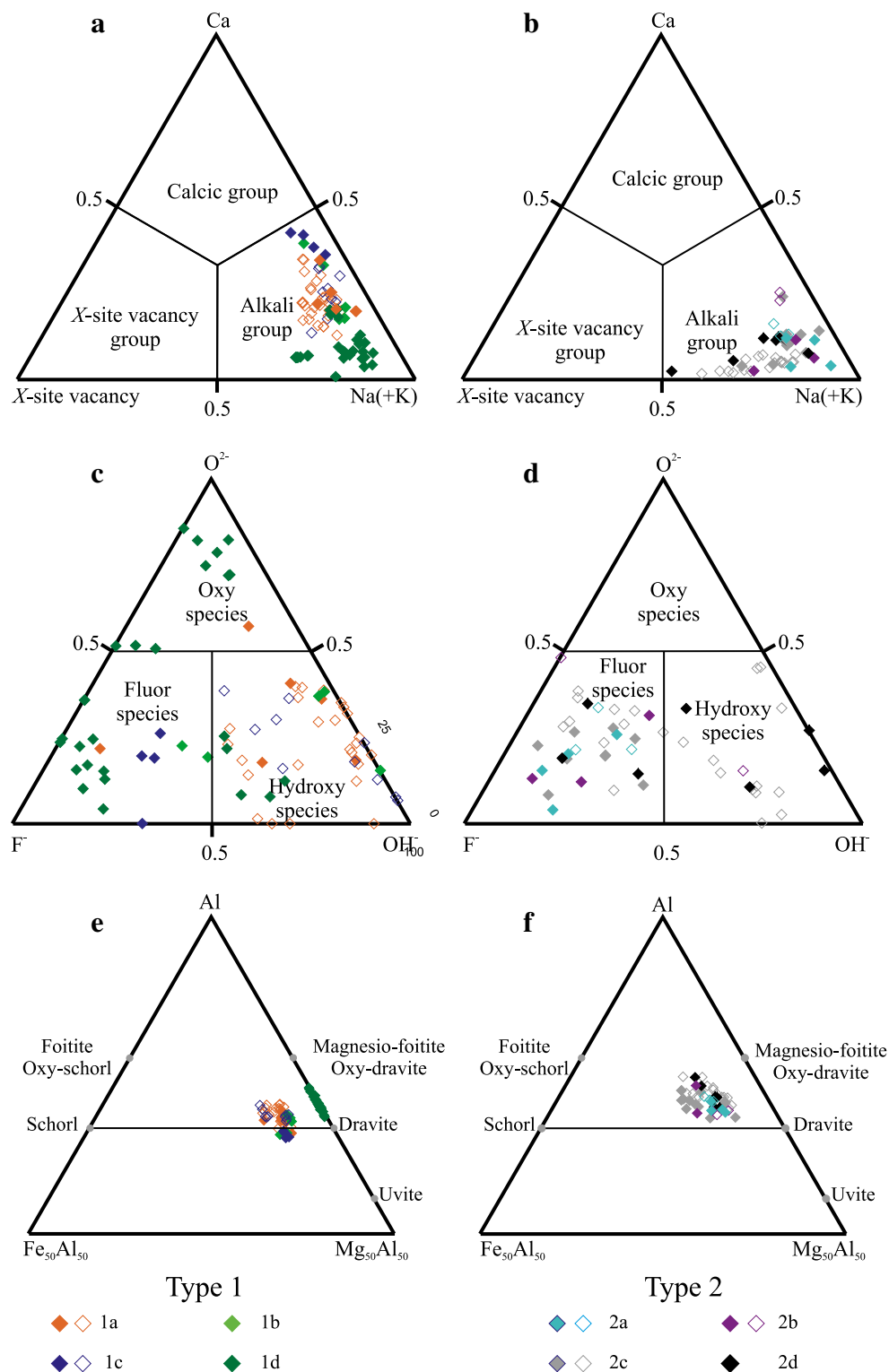
Fig. 5 Ternary plots illustrating the classification and chemical variations of type 1 tourmalines (*left-hand plots*) and type 2 tourmalines (*right-hand plots*) from the Mariinsky and Krasnoarmeisky deposits. The data shown combine analyses from this study (*solid symbols*) and published data (*unfilled symbols*) from Baksheev et al. (2003) and Kudryavtseva et al. (2004)

2. The plot of W-site anions F^{-}-O^{2-}-OH^{-} (Fig. 5c, d) shows an extreme spread of values, but only type 1 tourmaline extends into the field of oxy-species. In terms of the Y-site cations Al, Fe, and Mg (Fig. 5e, f), the two tourmaline groups show more restricted ranges that largely overlap, except for the nearly Fe-free type 1d tourmaline. Applying the tourmaline formula

calculation and classification of Henry et al. (2011), the tourmaline of types 1 correspond to dravite and fluor-dravite, except for some Cr-rich tourmaline of type 1d that classify as oxy-dravite and chromo-alumino-povondraite. Type 2 tourmaline classifies as dravite and fluor-dravite.

Type 1 tourmalines in all but the chromitite-related samples have moderate Fe/(Fe + Mg) ratios from 0.17 to 0.28, and contents of Ca, X-site vacancy proportion, and F from 0.17 to 0.43, from 0.05 to 0.19, and from 0.04 to 0.68 apfu, respectively (Table 1). Their Ti concentration varies from 0.02 to 0.18 apfu. Despite the association with emerald, the Cr contents of type 1a–1c tourmaline are very low, not exceeding 0.25 wt.%. The chromitite-related tourmaline of type 1d is compositionally distinct. The Fe and Ti contents are extremely low (Fe/(Fe + Mg) < 0.01), whereas the concentrations of Ca, F, and X-site vacancies are similar to the other type 1 varieties (Table 1). The Cr contents in type 1d tourmaline are variable and high, whereby two subgroups can be distinguished; one

with 0.17 to 1.08 Cr apfu and the other with values from 3 to 3.25 apfu. The highest published Cr content in tourmaline known to the authors (3.47 apfu) was measured in type chromo-alumino-povondraite from the Pereval quarry, Sludyanka, Baikal Region, Russia (Reznitskii et al. 2014). Therefore, the Cr contents in the type 1d Mariinsky tourmaline are among the highest reported in the literature. Finally, it is noted that the formulae for Cr-rich tourmaline indicate considerable O^{2-} at the W-site, whereas F and OH^- dominate in the other type 1d tourmaline.

The type 2 tourmalines studied here differ from those of type 1 in several ways. They have lower Ca contents (0.02 to 0.12 apfu with exceptions to 0.24; see Fig. 6), higher X-site vacancies (to 0.3 apfu; Table 1, Fig. 5b), and a greater range of Fe concentrations from 0.01 to 1.09 apfu. The range of F contents from 0.05 to 0.76 apfu is similar to that in type 1. The Cr contents are rarely above the detection limit (Table 1).
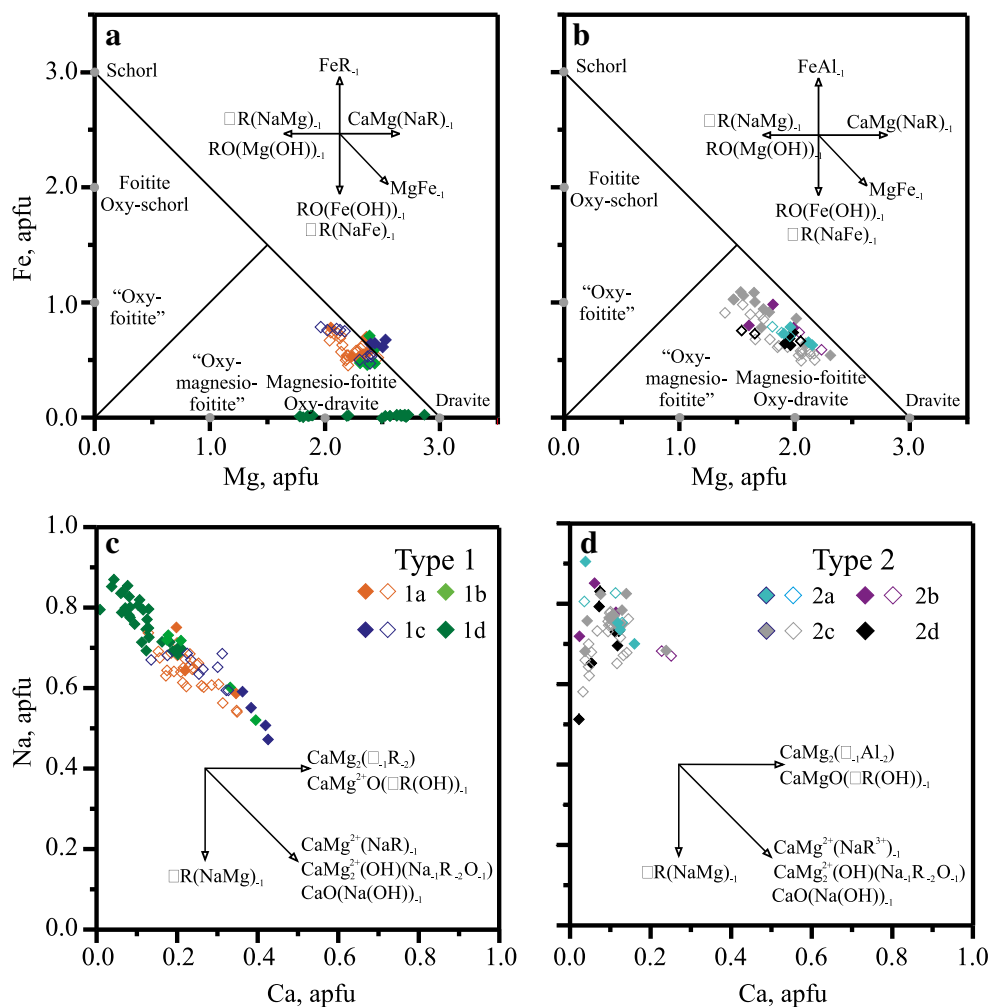

Fig. 6 Binary plots illustrating differences in isomorphic substitutions of Fe–Mg (**a**, **b**) and Na–Ca (**c**, **d**) in type 1 and 2 tourmalines from the Mariinsky and Krasnoarmeisky deposits, with potential exchange vectors shown for reference (R = Al^{3+}, Cr^{3+}). See Fig. 5 for the symbol explanation

Variation trends on binary plots of Fe–Mg and Na–Ca (Fig. 6) also point out significant differences in the two tourmaline types. The type 1 subgroups show different trends, some poorly defined, in the Fe–Mg plot, which suggest a variety of substitutions. In contrast, all type 2 tourmalines define a trend corresponding roughly to the $FeMg_{-1}$ vector. On the Na–Ca plot, type 1 tourmaline forms a single, well-defined trend parallel to three vectors $CaMg(NaR)_{-1}$, $CaMg_2(OH)(Na_{-1}R_{-2}O_{-1})$ where R = Al^{3+} or Cr^{3+}, or $CaO(NaOH)_{-1}$. Which vector can most likely be examined by comparing correlation coefficients for the respective components, for example Ca + Mg versus Na + R for $CaMg(NaR)_{-1}$? The results, when calculated separately for types 1a, 1b, and 1d (type 1c has too few data), are −0.80 to −0.95 for the first vector, −0.5 to −0.9 for the second, and −0.35 to −0.90 for the third. Therefore, we conclude that the coupled substitution Ca + Mg ↔ Na + R best reflects the variations in type 1 tourmaline. The Ca–Na trend for type 2b tourmaline is also parallel with the $CaMg(NaR)_{-1}$ vector whereas the rest of the type 2 compositions define a near-vertical trend suggesting the substitution X-site vacancy + R ↔ Na + Mg.

Trace elements

The trace element compositions of the Mariinsky tourmaline are grouped according to the host-rock type in Table 2. It is worth noting that trace element concentrations in type 1d tourmaline were measured only in grains corresponding to the first group (enriched in Ni and F, and comparatively depleted in Cr). In comparing the two groups of data, the first-order differences are that type 1 have relatively low concentrations of Zn and Co ranging from 24 to 195 and from bdl to 36 ppm compared with 256–796 and 42–90 ppm for type 2 (Fig. 7a, b). The Li content in type 1 tourmaline is also slightly lower (48–210 ppm) than in type 2 (100–409 ppm), but the ranges overlap. By contrast, the V and Sr contents in type 1 tourmaline are higher than those in type 2, whereas type 2 tourmalines are comparatively enriched in REE (Table 2, Fig. 7g, h). The Ni concentration in type 1a–1c tourmaline ranges from 31 to 614 ppm (Table 2). Type 1d tourmaline has much higher Ni contents (1350 to 1900 ppm). Type 2 tourmaline has Ni content from 178 to 1751 ppm (Table 2). Ni is positively correlated with Co in both tourmaline types (Fig. 7e, f), with correlation coefficients of 0.90 for type 1 (except 1d) and 0.87 for type 2.

The Be contents in tourmaline show no relationship to the presence or absence of beryl. In type 1 tourmaline coexisting with beryl or chrysoberyl-mariinskite solid solution, it ranges from 0.8 to 26 ppm (Table 2). The Be concentration in type 2a, 2c, and 2d tourmaline ranges from 8 to 13 ppm, and the highest Be content determined in this study, 45–54 ppm, is from type 2b tourmaline (Table 2). Galbraith et al. (2009) also found no difference in Be contents in tourmaline from

emerald-bearing and barren samples at the Tsa da Glisza deposit in Canada. Their values of 15–50 ppm compare well with the Mariinsky data reported here.

The total REE contents in Mariinsky tourmaline of all types are low, not exceeding 20 ppm except in type 2b (Table 2). The REE concentrations in type 2 tourmaline are generally higher than in type 1, but the distribution patterns for type 1 and 2 tourmaline are similar (Fig. 8a, b), with a relative enrichment in LREE over HREE (which are commonly below detection limit) and a strong positive Eu anomaly (Table 2). The REE distribution patterns in phlogopite (Bidny 2012) and in fluorite (Popov and Erokhin 2010) from Mariinsky are similar to those in tourmaline (Fig. 8a, b). Plots of total REE versus Sr (Fig. 7g, h) demonstrate contrary behavior of these variables in type 1 and 2 tourmaline. Thus, the type 1 tourmaline is enriched in Sr and depleted in REE, whereas the opposite is true for type 2 tourmaline.

Boron isotopic composition

The boron isotopic composition of tourmaline from all samples measured (34 analyses in 12 samples) is homogeneous, with a total range from −11.3 to −8.4‰ in $\delta^{11}B$ values. The average value is −10.1‰ (0.7 SD). There are no significant differences from one sample to another within the data set and within-grain variations are equal to or lower than the analytical uncertainty (0.7‰, see Table 3). Therefore, despite differences in mineral assemblage and the presence or absence of emerald mineralization in the samples, all type 1 and type 2 tourmaline have the same B-isotope composition (Table 3). Correlations between isotopic and chemical compositions are not striking and difficult to assess given the narrow range of $\delta^{11}B$ variation. The only notable correlation was found for $\delta^{11}B$ and Co in type 2 tourmaline (Fig. 9), with a correlation coefficient of 0.82, but in general the B-isotope and chemical compositions are not systematically linked.

Discussion and comparison with other emerald deposits

Controls on chemical variations in tourmaline

As demonstrated above, type 2 tourmalines are relatively enriched in Al compared with type 1 tourmaline, and they have lower Ca and Na contents with corresponding higher X-site vacancies. Some of the chemical variations can be explained by differences in the mineral assemblage and host-rock composition. Thus, although type 2 tourmalines have generally low Ca, the highest values, from type 2c, relate to phlogopite–plagioclase–tourmaline veins at the contact with gabbro and diorite dykes, which are enriched in that element. In other cases, lower Ca contents in type 2 tourmaline likely
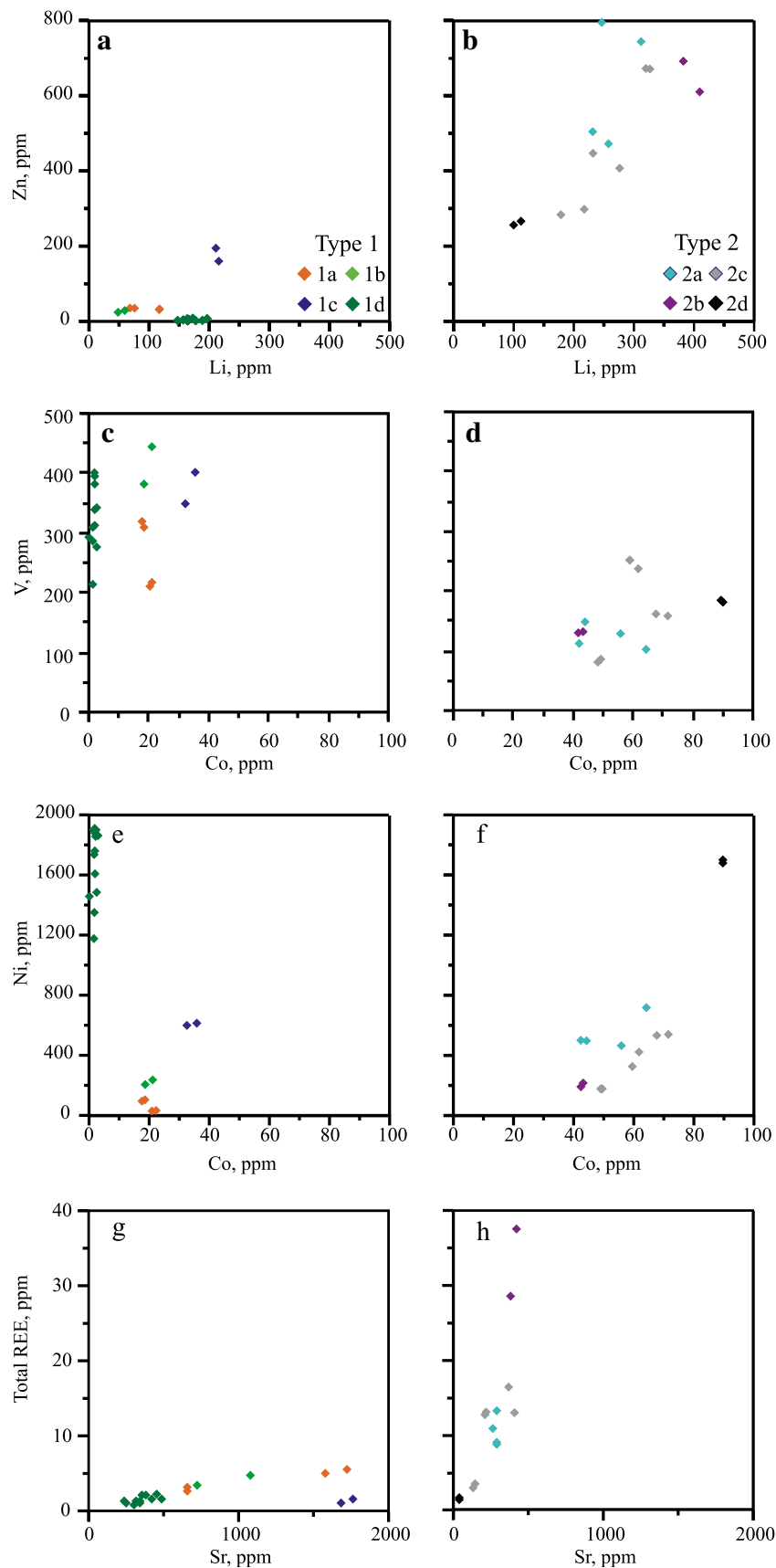
Fig. 7 Binary plots comparing the variations of selected trace elements in Mariinsky and Krasnoarmeisky type 1 and type 2 tourmalines. **a**, **b** Zn versus Li. **c**, **d** V versus Co. **e**, **f** Ni versus Co. **g**, **h** Total REE versus Sr. See text for explanation
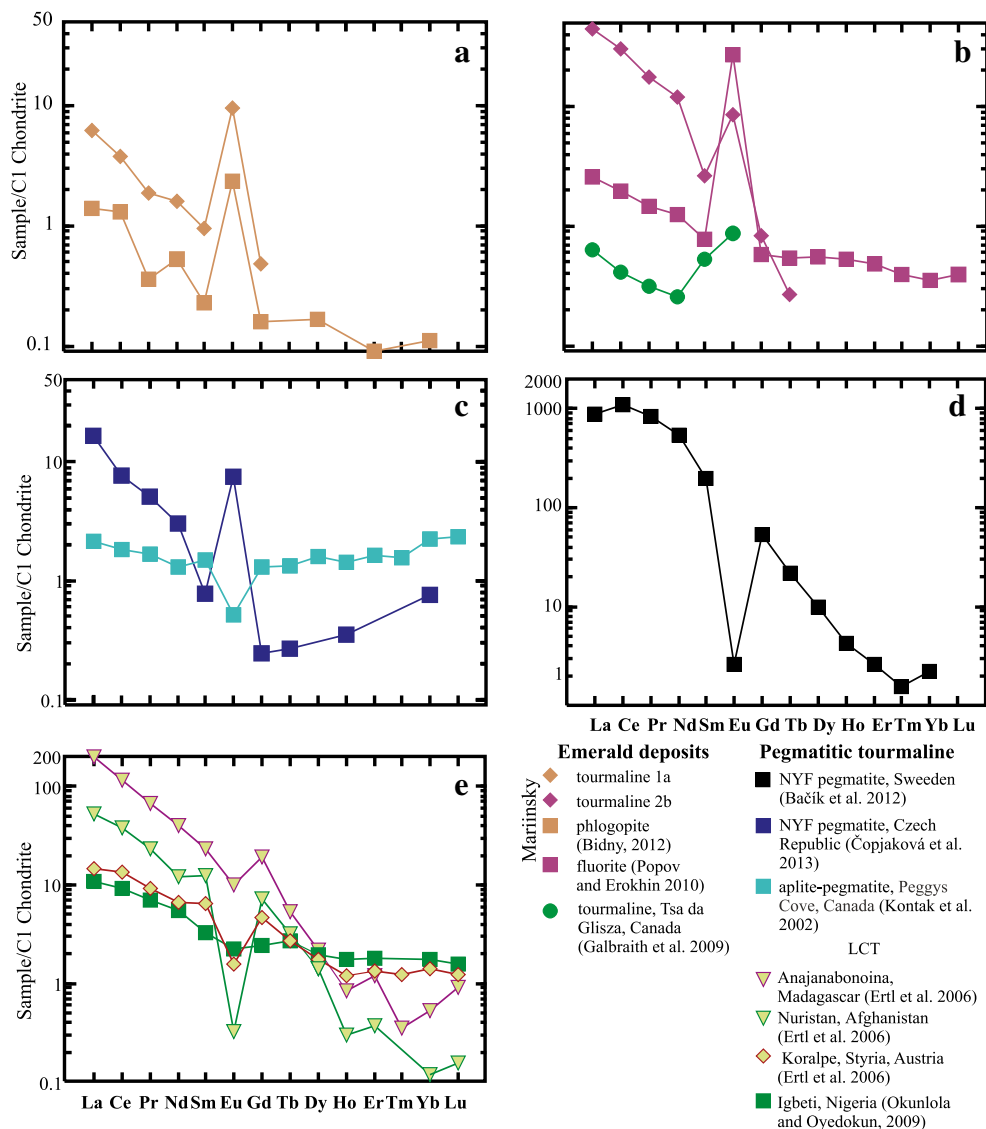
Fig. 8 C1-chondrite normalized REE distribution patterns of tourmaline from Mariinsky compared with published data from Tsa da Glisza emerald deposit, Canada, and tourmaline from various NYF- and LCT-type pegmatites. Plot **a** Mariinsky tourmaline 1a and phlogopite, **b** Mariinsky tourmaline 2b and fluorite with tourmaline from Tsa da Glisza, **c** tourmaline from NYF and aplite–pegmatite, **d** tourmaline from NYF pegmatite, **e** tourmaline from LCT pegmatites. The C1 chondrite data are from McDonough and Sun (1995)

relate to partitioning of that element to coexisting minerals like amphibole, fluorite, or margarite. In a similar way, low Na concentration in tourmaline from type 2d topaz–paragonite veinlets is attributed to Na partitioning into paragonite.

Figure 10 shows comparisons of the Mariinsky tourmaline with those of other schist-hosted emerald deposits in the literature. The Ca and Na contents in tourmaline from other deposits are similar to those from emerald-bearing (type 1) tourmaline at Mariinsky, and most plot along a similar trend, parallel with the $CaMg(NaR^{3+})_{-1}$ exchange vector (Fig. 10a, b). The exception is Ca-poor tourmaline from Swat, which Arif et al. (2010) noted are from late veins and veinlets associated with carbonate minerals. Those post-mineralization Swat

tourmaline form a vertical array on Fig. 10b, parallel with the $\square R^{3+}(NaMg)_{-1}$ exchange vector like the late type 2 tourmaline from Mariinsky. Thus, our study shows different types of isomorphic substitutions for tourmaline from emerald-bearing and emerald-free veins, which may be of use in exploration.

The literature data show that tourmaline from schist-hosted emerald deposits clearly related to granitic rocks is enriched in F similar to the Mariinsky tourmaline. Examples are Tsa da Glisza, Canada (Groat et al. 2002), with F up to 0.72 apfu; Crabtree, Canada, with up to 0.75 apfu (Clark et al. 2011); and Khaltaro, Pakistan, with up to 0.79 apfu (Laurs et al. 1996). There are no fluorine data reported for tourmaline in the
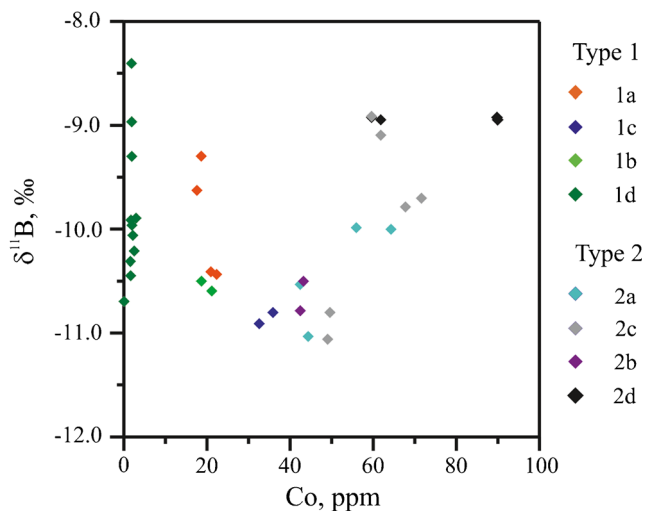
Fig. 9 A binary plot of $\delta^{11}B$ versus Co concentration in tourmaline from the Mariinsky deposit, showing a positive correlation for the type 2 tourmaline data

Trace elements

It is suggested that variations in Li and Zn in the Mariinsky tourmaline can be related to the presence or absence of phlogopite. Type 1 tourmaline in phlogopite-rich veins are relatively depleted in these elements, whereas type 2 tourmaline in assemblages with margarite, paragonite, plagioclase, and fluorite have higher Li and Zn contents. This is consistent with preferential partitioning of Li and Zn in dark mica. According to Bidny (2012), the Li and Zn contents in phlogopite from the Mariinsky deposit reach 4000 and 610 ppm, respectively, much higher than in tourmaline. The Li and Zn contents in tourmaline from altered ultramafic host rocks and ultramafic-hosted quartz–tourmaline veins at the Tsa da Glisza prospect in Canada are similar to Mariinsky type 1 tourmaline, ranging from 61 to 132 ppm and 59 to 224 ppm, respectively (Galbraith et al. 2009). However, total variations in Li and Zn contents in the Tsa da Glisza tourmaline are much wider (Fig. 10c), which is probably caused by various host rocks at this deposit. It is worth noting that the Tsa da Glisza

granite-related Kafubu deposit in Zambia, but phlogopite associated with tourmaline from that area contains up to 4.7 wt.% F (Seifert et al. 2004), similar to Mariinsky, where phlogopite in type 1 veins contains up to 3.9 wt.% F (Baksheev et al. 2003). There are few published analyses from emerald deposits lacking a granite or pegmatite association, but one example is the Habachtal deposit, Austria, whose tourmaline has very low F contents (up to 0.2 apfu; Trumbull et al. 2009). From this limited number of studies, it seems that the F content in tourmaline may be useful to distinguish the influence of granitic or pegmatite fluids in schist-hosted emerald deposits.

tourmaline displays a positive correlation between Li and Zn similar to the Mariinsky tourmaline (Fig. 10c). The lower Ni and Co contents in type 1 versus type 2 tourmaline may also reflect partitioning of these elements into phlogopite. Bidny (2012) reported Ni and Co concentrations in Mariinsky phlogopite of 525 and 47 ppm, respectively. The highest Ni content in Mariinsky tourmaline is from the type 1d alteration zone where tourmaline replaces chrome spinel, the assumed Ni source. Ni-rich phlogopite is also present, but formed after tourmaline. The V and Co contents in the Mariinsky and Tsa da Glisza tourmaline are similar (Fig. 10d).

Data on REE abundance and patterns in tourmaline from schist-hosted emerald deposits are so far limited to the Tsa da Glisza example, Canada. Galbraith et al. (2009) reported very low concentration of REE from tourmaline of the Tsa da Glisza prospect (total REE a few ppm) that are similar to the Mariinsky tourmaline reported here (Fig. 8b). The low REE contents for Mariinsky tourmaline could reflect a derivation of these elements from the ultramafic host rocks. However, according to Erokhin (2006), REE contents in fresh ultramafic rocks of the Bazhenovsky Complex to which ultramafics of the emerald belt belong is about ten times lower (0.5–0.6 ppm) than in the tourmaline, which suggests that REE were derived from a different and potentially granitic source. A granitic or pegmatitic source is commonly invoked for explaining the source of Be needed to form emerald in ultramafic rocks (e.g., Groat et al., 2008), and it may also be the source of boron and other components for tourmaline formation in these rocks. Thus, it is worth comparing the REE patterns of Mariinsky tourmaline with those from pegmatite-hosted tourmalines, including both NYF (Nb-Y-F) and LCT (Li-Cs-Ta) types (Fig. 8). The comparison shows that REE patterns in tourmaline from schist-hosted emerald deposits are quite similar to that of the NYF pegmatite-hosted tourmaline from the Czech Republic, especially the low concentrations, steep LREE to MREE slope, and strong positive Eu anomaly. The tourmalines from LCT pegmatites and aplites have quite different REE patterns (Fig. 8c, d). The Eu anomaly is commonly negative in the pegmatite and aplite tourmalines, which is expected for a residual granitic melt that crystallized feldspar. However, the interpretation of positive Eu anomalies is not so straightforward. Note that tourmaline from pegmatite from Forshammar in Sweden (Bačik et al. 2012) has a positive anomaly, and the opposite is found in tourmaline from pegmatite in the Třebíč Pluton in Czech Republic (Čopjaková et al. 2013), both of S-type (Fig. 8c, d). The oxygen fugacity can influence the behavior of Eu by controlling the proportions of trivalent versus divalent Eu, whereby only the latter is able to substitute for Ca and produce a negative anomaly by feldspar fractionation. This is expected for common crustal oxygen fugacities near the QFM buffer, but more oxidizing environments do not produce a positive Eu anomaly. Instead, trivalent Eu simply follows the geochemical behavior of
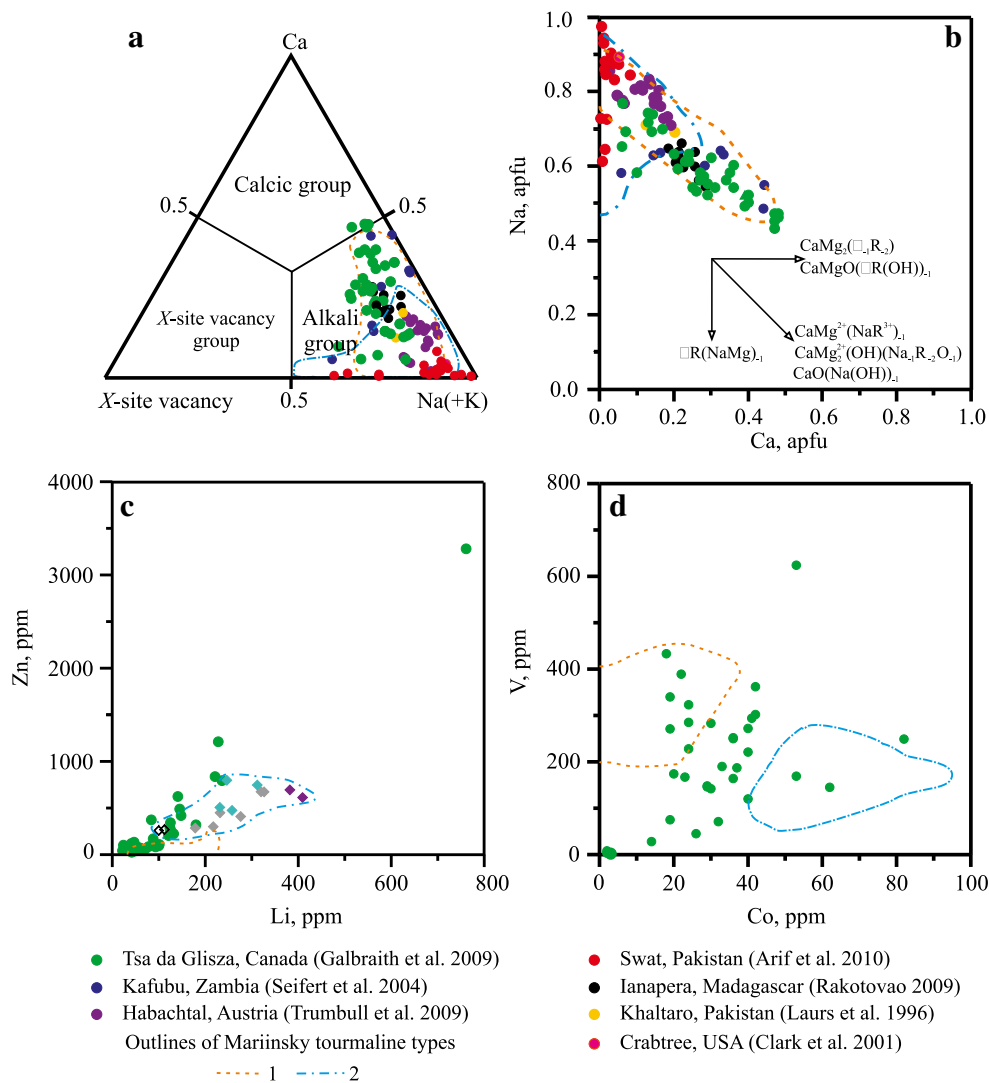
Fig. 10 Ternary and binary plots comparing the major and trace element composition of tourmalines from other schist-hosted emerald deposits with the fields for Mariinsky tourmaline (*dashed lines*, *red* for type 1 and *blue* for type 2). Several exchange vectors for Ca–Na are plotted in plot (**b**) for reference (R = Al^{3+}, Cr^{3+})

neighboring trivalent REEs Sm and Gd, and there is no anomaly. More likely is that the positive Eu anomaly in tourmalines reflects a hydrothermal fluid composition, enriched in Eu due to replacement of igneous plagioclase by sericite or albite with a release of Ca and Eu to the fluid.

Lithium contents in the Mariinsky tourmaline reach a few hundred ppm, which is close to that in NYF-type pegmatitic tourmaline (Novák et al. 2011; Bačik et al. 2012), whereas the Li concentration in the LCT-type tourmaline can be much higher.

Based on the above discussion of element concentrations and comparison with literature data, we suggest that the Mariinsky tourmaline originated from the interaction of ultramafic rocks and a boron-rich fluid derived from associated pegmatites and/or their source granites. By analogy, the same might be true for the origin of beryl mineralization manifested by emeralds in the same rocks.

Major and trace elements as exploration guides

Galbraith et al. (2009) reported that tourmaline composition might be used in the exploration for the schist-hosted emeralds. Our study supported that suggestion in general. At the same time, we found criteria allowing distinction of tourmaline from emerald-bearing and emerald-free veins at the schist-hosted deposits worldwide. The former is dominated by the uvite-type isomorphic substitution, whereas the latter has vacancy-type substitution. In addition, we established some features of trace element behavior in tourmaline from emerald-bearing and emerald-free veins, which could be applied as exploration guides within the Ural emerald mining district. Tourmaline from the emerald-bearing veins is enriched in Sr and V and depleted in REE and Co, whereas tourmaline from emerald-free veins displays the opposite behavior. Owing to the
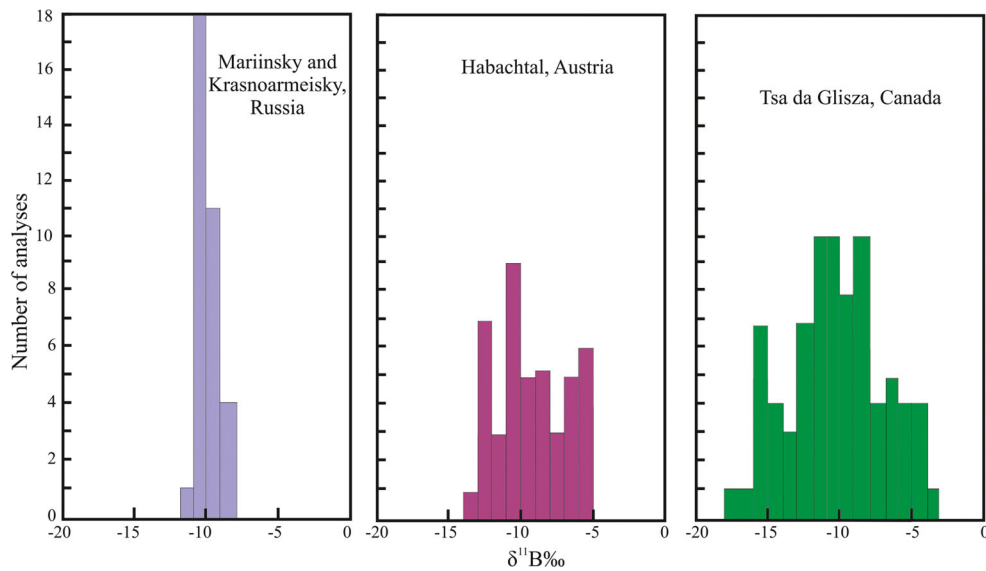
Fig. 11 Histograms comparing the δ^{11}B values of tourmaline from the Mariinsky and Krasnoarmeisky emerald deposits (this study) with tourmaline from other schist-hosted emerald deposits. Data for Habachtal, Austria, and Tsa da Glisza, Canada, are from Trumbull et al. (2009) and Galbraith et al. (2009), respectively. Note the very narrow range of B-isotope composition from the Urals localities compared with the other examples

association with phlogopite, tourmaline from emerald-bearing veins is depleted in Zn, whereas that from emerald- and phlogopite-free veins is enriched in this element.

Boron isotopes and implications for fluid source

Before attempting to interpret the tourmaline B-isotope compositions in terms of source, it is necessary to account for the tourmaline-fluid isotope fractionation, which is dependent on temperature. Baksheev et al. (2003) and Kudryavtseva et al. (2004) estimated the formation temperature of tourmaline from phlogopite–tourmaline veins (corresponding to type 1a tourmaline in this study) and margarite veinlets (corresponding to type 2c tourmaline in this study) from the tourmaline–biotite thermometer of Colopietro and Frieberg (1987) as 410–420 °C and 350–360 °C, respectively. The complexity of tourmaline crystal chemistry makes application of the Fe–Mg exchange thermometry problematic, and these estimates are to be treated with caution. In any case, the B-isotope fractionation between tourmaline and aqueous fluid favors ^{11}B in the fluid phase. For a reference temperature of 400 °C that seems reasonable from the available data, the tourmaline-fluid fractionation factors of Meyer et al. (2008) predict a fluid composition 2.7‰ heavier than tourmaline, i.e., −8.6 to −5.7‰. A difference in 50 °C in the temperature corresponds to a 0.5‰ difference in the fractionation effect.

Given these estimates for the fluid B-isotope composition, potential B sources for the tourmaline formation at the Mariinsky deposit are serpentinized ultramafic rocks of mantle origin, mafic (diorite) igneous dykes, also of mantle origin, and the crustal granites of Kamenka, Adui, and related pegmatite

intrusions. The proximity and abundance of granites in and around the Urals emerald belt, the relatively high F and Li contents in Mariinsky tourmaline, and the REE distribution pattern and concentrations in tourmaline (see above) suggest that a contribution of boron from a granitic source is likely. There is no information on the B-isotope composition of the country rocks in the Mariinsky deposit, but extensive compilations of B-isotope data for fresh and submarine-altered mid-ocean ridge basalt (MORB), serpentinites, and crustal granites worldwide (e.g., Marschall and Jiang 2011; Trumbull et al. 2013; Farber et al. 2015; Marschall et al. 2017) give a good basis for comparison. From these compilations, the expected δ^{11}B values of crustal (S-type) granitic magmas (and high-temperature fluids derived from them) are in the range of −8 to −12‰. Mantle-derived boron composition is best represented by the global average for MORB, which when fresh has a narrow range of B-isotope compositions with δ^{11}B of −7 ± 1‰ (Marschall et al. 2017). Fresh mafic intrusive rocks are rare in the Emerald mines district (only a few mafic dykes occur) and their expected boron concentrations are low (around 1 ppm for MORB; Marschall et al. 2017). Seawater-altered oceanic crust and serpentinites contain significantly higher B concentrations than fresh basalt, and their B-isotope composition are considerably heavier than −5‰ (Smith et al. 1995). Taking these factors into account, we favor a mixed source of boron to account for the estimated Mariinsky fluid composition of about −6 to −9‰. The unknown composition of wall-rock boron and the uncertainty in tourmaline formation temperature do not allow a good estimate of mixing proportions, but the narrow range of B-isotope compositions in tourmaline of all types indicates a well-mixed hydrothermal system and high fluid/rock ratios.

Studies of tourmaline B-isotopes from other schist-hosted emerald deposits are not abundant, but the examples from Habachtal, Austria (Trumbull et al. 2009), and Tsa da Glisza, Canada (Galbraith et al. 2009), both revealed a much larger range of $\delta^{11}B$ values than at Mariinsky (Fig. 11), and both concluded a mixed source, with isotopically heavy boron from mafic–ultramafic rocks on the one hand and pelitic metasedimentary rocks (Habachtal) or granites (Tsa da Glisza) on the other. A mixed fluid source for boron is of course consistent with overall geochemical model for schist-hosted emerald formation, which requires bringing together a source of the lithophile, highly incompatible element Be, and a peraluminous system to form beryl, as well as the siderophile and highly compatible element Cr which is needed to produce the variety emerald.

Conclusions

Tourmaline is a common mineral in the Mariinsky schist-hosted emerald deposit in the Middle Urals, Russia. Two types of tourmaline that differ in their geological position, isomorphic substitutions, and trace element concentrations are recognized. The type 1 tourmalines (dravite, fluor-dravite, oxy-dravite, or chromo-alumino-povondraite) are found in emerald-bearing phlogopite veins and type 2 tourmalines (dravite, fluor-dravite, or oxy-dravite) are hosted in later emerald-free pockets, lenses, and veinlets cutting the phlogopite veins. These types differ in their isomorphic substitutions. The Ca + Mg $\leftrightarrow$ Na + R and R + O $\leftrightarrow$ Mg + OH (R = Al^{3+}, Cr^{3+}) substitutions dominate in type 1 tourmaline, whereas type 2 tourmaline are characterized by the coupled substitutions Mg $\leftrightarrow$ Fe and X-site vacancy + Al $\leftrightarrow$ Na + Mg. The major and trace element composition with exception of REE, Li, and Be of the both tourmaline types is influenced by replaced host rocks, associated mineral, and minerals crystallized before. Mariinsky tourmaline originated from the interaction of ultramafic rocks and a boron-rich fluid derived from associated pegmatites and/or their source granites. The boron isotopic composition of tourmaline is nearly the same in all rock types (−11.3 to −8.4‰). Based on tourmaline-fluid isotopic fractionation at an estimated formation temperature of 400 °C, the fluid B-isotope composition is estimated to be −8.6 to −5.7‰. To explain that value, a mixed source of boron is proposed, with a granitic component and a significant contribution from metamorphosed mafic–ultramafic host rocks.

References

Arif M, Fallick AE, Moon CJ (1996) The genesis of emeralds and their host rocks from Swat, northwestern Pakistan: a stable-isotope investigation. Mineral Deposita 31:255–268

Arif M, Henry DJ, Moon CJ (2010) Cr-bearing tourmaline associated with emerald deposits from Swat, NW Pakistan: genesis and its exploration significance. Am Mineral 95:799–809

Bačík P, Uher P, Ertl A, Jonsson E, Nisten P, Kanický V, Vacullovivič T (2012) Zoned REE-enriched dravite from a granitic pegmatite in Forshammar, Bergslagen province, Sweden: an EMPA, XRD and LA-ICP-MS study. Can Mineral 50:825–841

Baksheev IA, Kudryavtseva OE, Belyatsky BV, Popov MP, Sarantseva NP, Vydrin MV (2003) Tourmaline-bearing alterations of the Ural emerald mines. Part II. Phlogopitite. Ural Geol J 4:3–34 (in Russian)

Baksheev IA, Kudryavtseva OE, Firsova NP, Popov MP (2002) Tourmaline-bearing alterations of the Ural emerald mines. Part I. Early albite–tourmaline–amphibole alteration. Ural Geol J 4:25–34 (in Russian)

Beus AA (1966) Geochemistry of beryllium and genetic types of beryllium deposits. Freeman, San Francisco

Bidny AS, Baksheev IA, Popov MP (2011) Rb–Sr systematics of beryl-bearing phlogopite schists at the eastern contact of the Murzinka–Adui granite complex, Urals. Litosfera 6:141–145 (in Russian)

Bidny AS (2012) Mineralogy, age, and genesis of beryl occurrences in the Ural emerald belt. Dissertation, Moscow State University (in Russian)

Catanzaro EJ, Champion CE, Garner EL, Malinenko G, Sappenfield KM, Shields WR (1970) Boric acid: isotopic and assay standard reference materials. US National Bureau Standards, Washington, D.C Special Publication 260-17

Clark CM, Hawthorne FC, Ottolini L (2011) Fluor-dravite, $NaMg_3Al_6Si_6O_{18}(BO_3)_3(OH)_3F$, a new mineral species of the tourmaline group from the Crabtree emerald mine, Mitchell County, North Carolina: description and crystal structure. Can Mineral 49: 57–62

Colopietro MR, Frieberg LM (1987) Tourmaline-biotite as a potential geothermometer for metapelites; Black Hills, South Dakota. Geol Soc Amer Abstracts with Programs 19(7):624

Čopjaková R, Škoda R, Vašinová-Galiová M, Novák M (2013) Distributions of Y + REE and Sc in tourmaline and their implications for the melt evolution; examples from NYF pegmatites of the Třebíč pluton, Moldanubian zone, Czech Republic. J Geosci 58: 113–131

Dutrow BL, Henry DJ (2000) Complexly zoned fibrous tourmaline, Cruzeiro mine, Minas Gerais, Brazil: a record of evolving magmatic and hydrothermal fluids. Can Mineral 38:131–143

Dyar MD, Wiedenbeck M, Robertson D, Cross LR, Delaney JS, Ferguson K, Francis CA, Grew ES, Guidotti CV, Hervig RL, Hughes JM, Husler J, Leeman W, McGuire AV, Rhede D, Rothe H, Paul RL, Richards I, Yates M (2001) Reference minerals for microanalysis of light elements. Geostand Newslett 25:441–463

Ertl A, Hughes JM, Prowatke S, Ludwig T, Prasad PSR, Brandstätter F, Körner W, Schuster R (2006) Tetrahedrally coordinated boron in tourmaline from the liddicoatite-elbaite series from Madagascar: structure, chemistry, and infrared spectroscopic studies. Am Mineral 91:1847–1856

Erokhin YuV (2006) Mineralogy of the Bazhenovsky ophiolite complex. Dissertation, Inst Geol Geochem Russ Acad Scie, Yekaterinburg (in Russian)

Farber K, Dziggel A, Trumbull RB, Meyer FM, Wiedenbeck M (2015) Tourmaline B-isotopes as tracers of fluid sources in silicified Palaeoarchean oceanic crust from the Mendon formation, Barberton greenstone belt, South Africa. Chem Geol 417:134–147

Fersman AE (1925) Gems of the USSR. Vol. 2 ANSSSR, Leningrad, p. 123–228 (in Russian)

Fershtater GB, Krasnobaev AA, Bea F, Montero P, Borodina NS (2007) Geodynamic settings and history of the Paleozoic intrusive magmatism of the central and southern Urals: results of zircon dating. Geotectonics 41:465–486

Galbraith CG, Clarke BD, Trumbull RB, Wiedenbeck M (2009) Assessment of tourmaline compositions as an indicator of emerald mineralization at the Tsa da Glisza prospect, Yukon territory, Canada. Econ Geol 104:713–731

Gavrilenko E. (2003) Esmeraldas de los Urales (Rusia): condiciones de formación y caracterización comparativa con las Esmeraldas de otros orígenes. Master thesis, Univ Politécn Madrid

Ginzburg AI (1959) Pneumatolithic-hydrothermal beryllium deposits. In: Geology of rare element deposits Moscow 4:4–13 (in Russian)

Giuliani G, Silva LJHD, Couto P (1990) Origin of emerald deposits of Brazil. Mineral Deposita 25:57–64

Groat LA, Giuliani G, Marshall DD, Turner D (2008) Emerald deposits and occurrences: a review. Ore Geol Rev 34:87–112

Groat LA, Marshall DD, Giuliani G, Murphy DC, Piercey SJ, Jambor JL, Mortensen JK, Ercit TS, Gault RA, Mattey DP, Schwarz D, Maluski H, Wise MA, Wengzynowsk W, Eaton DW (2002) Mineralogical and geochemical study of the Regal Ridge emerald showing, southeastern Yukon. Can Mineral 40:1313–1338

Grundmann G, Morteani G (1989) Emerald mineralization during regional metamorphism: the Habachtal (Austria) and Leydsdorp (Transvaal, South Africa) deposits. Econ Geol 84:1835–1849

Henry DJ, Novák M, Hawthorne FC, Ertl A, Dutrow BL, Uher P, Pezzotta F (2011) Nomenclature of the tourmaline-supergroup minerals. Am Mineral 96:895–913

Jarosewich E (2002) Smithsonian microbeam standards. J Res Natl Inst Stand Technol 107(6):681–685

Khiller VV, Popov MP, Erokhin YV, Zakharov AV (2015) Th-U-Pb-age of rare-metal granitic pegmatites at eastern contact of Adui pluton, central Urals, Russia. Bull Voronezh Univ Ser Geol 4:61–65 **(in Russian)**

Kontak DJ, Dostal J, Kyser TK, Archibald DA (2002) A petrological, geochemical, isotopic and fluid-inclusion study of 370 ma pegmatite–aplite sheets, Peggys Cove, Nova Scotia, Canada. Can Mineral 40:1249–1286

Kudryavtseva OE, Baksheev IA, Popov MP, Ustinov VI (2004) Tourmaline-bearing alterations of the Ural emerald mines. Part III. Tourmaline-margarite veinlets with albite, phlogopite, and chlorite. Ural Geol J 3:51–68 (in Russian)

Kupriyanova II (2002) On the genesis of the Malyshevsk beryllium-emerald deposit (middle Urals, Russia). Geol Ore Deposits 44:276–290

Kupriyanova II, Sokolov SV (1984) Formation conditions of phlogopite-beryllium mineralization. Geol Rudn Mestorozhd 26(6):32–44 (in Russian)

Laurs BM, Dilles JH, Snee LW (1996) Emerald mineralization and metasomatism of amphibolite, Khaltaro granitic pegmatite–hydrothermal vein system, Haramosh Mountains, northern Pakistan. Can Mineral 34:1253–1286

Longerich HP, Jackson SE, Günther D (1996) Laser ablation inductively coupled plasma mass spectrometric transient signal data acquisition and analyte concentration calculation. J Anal At Spectrom 11:899–904

Marschall HR, Jiang SY (2011) Tourmaline isotopes: no element left behind. Elements 7:313–319

Marschall HR, Wanless VD, Shimizu N, Pogge von Strandmann PAE, Elliot T, Monteleone BD (2017) The boron and lithium isotopic composition of mid-ocean ridge basalt and the mantle. Geochim Cosmochim Acta 207:102–138

McDonough WF, Sun S-s (1995) The composition of the earth. Chem Geol 120:223–253

Meyer C, Wunder B, Meixner A, Romer RL, Heinrich W (2008) Boron isotope fractionation between tourmaline and fluid: an experimental re-investigation. Contrib Mineral Petrol 156:259–267

Novák M, Škoda R, Filip J, Macek I, Vaculovič T (2011) Compositional trends in tourmaline from intragranitic NYF pegmatites of the Třebíč pluton, Czech Republic: an electron microprobe, Mössbauer and LA–ICP–MS study. Can Mineral 49:359–380

Okunlola OA, Oyedokun MO (2009) Compositional trends and rare metal (Ta-Nb) mineralization potential of pegmatite and associated lithologies of Igbeti area, southwestern Nigeria. RMZ - Mater Geoenvir 56:38–53

Popov MP (2014) Geological and mineralogical features of rare metal mineralization at the eastern contact of the Adui pluton within the Ural emerald belt. Ural State Min Univ, Yekaterinburg, 142 pp (in Russian)

Popov MP, Erokhin YV (2010) Typical features of fluorite from the Mariinsky beryllium deposit, Ural emerald mines. Litosfera 4: 157–162 (in Russian)

Popov MP, Zhernakov VI, Zolotukhin FF, Samsonov AV (2008) Ural emerald mines. Ural State Min Univ, Yekaterinburg (in Russian)

Popov VS, Bogatov VI, PetrovaAYu BBV (2003) Age and possible sources of granites from the Murzinka-Adui block, the central Urals: Rb–Sr and Sm–Nd isotopic evidence. Litosfera 4:3–18 (in Russian)

Rakotovao AP (2009) Contexte géologique et métallogénique des minéralisations en émeraude du gisement de Ianapera, bloc du Vohibory, Sud-Ouest de Madagascar. Dissertation, l'Université de Toulouse III-Paul Sabatier

Reznitskii L, Clark CM, Hawthorne FC, Grice JD, Skogby H, Hålenius U, Bosi F (2014) Chromo-alumino-povondraite, $NaCr_3(Al_4Mg_2)(Si_6O_{18})(BO_3)_3(OH)_3O$, a new mineral species of the tourmaline supergroup. Am Mineral 99:1767–1773

Schmid S (2001) The geology and genesis of the 'Kandemwa' emerald deposit in Zimbabwe, Africa. EUG XI 2001. Abstracts with Program, p. 548

Seifert AV, Žáček V, Vrána S, Pecina V, Zachariáš J, Zwaan JC (2004) Emerald mineralization in the Kafubu area, Zambia. Czech Geol Surv Bull Geosci 79:1–40

Sherstyuk AI, Kozlov VA (1976) Microthermometry of fluid inclusions in the Ural emeralds. Proc Sverdlovsk Mining Inst 124:42–48 (in Russian)

Smith HJ, Spivack AJ, Staudigel H, Hart SR (1995) The boron isotopic composition of altered oceanic crust. Chem Geol 126:119–135

Spiridonov EM (1998) Gemstone deposits of the former Soviet Union. J Gemmol 26:111–125

Trumbull RB, Krienitz M-S, Grundmann G, Wiedenbeck M (2009) Tourmaline geochemistry and $\delta^{11}B$ variations as a guide to fluid–rock interaction in the Habachtal emerald deposit, Tauern window, Austria. Contrib Mineral Petrol 157:411–427

Trumbull RB, Beurlen H, Wiedenbeck M, Soares DR (2013) The diversity of B-isotope variations in tourmaline from rare-element pegmatites in the Borborema Province of Brazil. Chem Geol 352:47–62

Vlasov KA, Kutukova EI (1960) Emerald mines. AN SSSR, Moscow 251 pp (in Russian)

Zachariáš J, Žáček V, Pudilová M, Machovič V (2005) Fluid inclusions and stable isotope study of quartz-tourmaline veins associated with beryl and emerald mineralization, Kafubu area, Zambia. Chem Geol 223:136–152

Zhernakov VI (1998) Topaz-paragonite metasomatic complexes of the Mariinsky emerald deposit. In: Geology of metamorphic complexes. USMGA, Yekaterinburg, pp. 94–101 (in Russian)

Zhernakov VI (2009) Ural emerald mines (notes on mineralogy). Mineral Almanac 14(2):7–125

Zolotukhin FF (1999) Regularities of the emerald distribution in the Malyshevskoe deposit. Geol Ore Deposits 41:398–413

Zolotukhin FF (1996) Mariinsky (Malyshevo) emerald deposit. St. Petersburg State Univ, St. Petersburg (in Russian)